Dynamic analysis of cylindrical shells subject to multiple blasts using FSI

N Mehreganian[1,2], G K Boiger[3], M Moatamedi[4,5], A S Fallah[4*]

1. Department of Civil & Environmental Engineering, University of Massachusetts Dartmouth, North Dartmouth, MA, USA

2. Creative Design Engineering Lab (Cdel), Department of Mechanical, Materials, and Aerospace Engineering, School of Engineering, University of Liverpool, Liverpool, UK

3. ICP Institute of Computational Physics, School of Engineering, Zürich University of Applied Sciences, Winterthur, Switzerland

4. Department of Mechanical, Electronic, and Chemical Engineering, Oslo Metropolitan University, Norway

5. Al Ghurair University, Dubai, UAE

ABSTRACT

Localised pressure pulse loads can pose a significant threat to structural elements as well as critical equipment and may cause failure and damage in the target due to the concentrated energy delivered upon a localised area of the target. The impulse impinged upon the localised zone at the contact interface can exceed 80% of the total impulse that the charge can deliver to the infinite target, leading to potential perforation of the structural element. When multiple charges are detonated, the advection of gaseous products depends, among other parameters such as fluid density, mass, and shape, on the type of blast wave interference and superposition.

This work examines the influence of multiple charge detonations blasted in the air on the external surface of cylindrical shells. Two types of detonations were considered, viz. simultaneous and sequential. In both cases the charges were positioned at 50mm and 75mm stand-off to the right and left of the shell. The Fluid-Structure Interaction (FSI) phenomenon was investigated in each scenario. The pressure registered with the gauge points of the rigid target was implemented in an uncoupled study on a flexible target which demonstrated different mode shapes occurring in the shell due to each blast scenario.

A dimensionless impulse parameter was defined based on the Gaussian distribution function associated with the load shape, which renders the probability of the impulse as the total impulse that can potentially be imparted to the target.

1. INTRODUCTION

Extensive pressure loads, such as those from the detonation of explosives proximal to structural elements, pose a significant threat to various components such as plates and shells.

*Corresponding Author: arashsol@oslomet.no

The phenomenological physics of blast pressure advection in the air and water gives rise to scenarios in each media, respectively, as (i) the shockfront which compresses the air and generates the incident wave, and (ii) the initial shock followed by bubble pulsation in underwater explosion events. The subsequent interaction of these loads with the structural frameworks, referred to as the fluid-structure interaction (FSI) along with superposition of waves and constructuve interference renders the dynamics of such extensive events inherently complex. For instance, the overpressure generated by the reflection of a blast from the target can reach twice the incident wave [1]–[3].

Although a multitude of research is available on the performance of structural frameworks subjected to such extensive pulse pressure loads [4]–[11], these methods have prevalently utilized the classical approaches and failed to account for the nonlinear compressibility effects and the FSI phenomenon. Various other studies in the literature have investigated blast loads experimentally [12]–[14], numerically [15]–[19], and analytically [20]–[26] addressing the effects of stand-off [27]–[29], charge type, mass, geometry [30]–[33].

Cylindrical shells have been ubiquitously used in the automotive, aerospace, and renewable energy wind power industries [34]–[39]. Onshore and offshore wind turbines utilise hollow cylindrical shells made of concrete or steel for the pylon. Due to the extra complications in the hydrodynamic and aerodynamic performance and physics of the wind turbine operation, the design of such structural frameworks is fraught with difficulty when dealing with these loading conditions, also requires further considerations to maintain a reasonable lifespan of structural components in the event of extreme loading.

In the event of multiple blasts detonated simultaneously or sequentially, the imparted impulse depends not only on the charge type, geometry, shape of the charges, stand-off distance, and the target shape, but also the interaction of the transmitted (and reflected) waves from each charge (and target) leading to constructive and destructive interferences. The objective of this study is therefore to investigate the influence of multiple blast scenarios on cylindrical shells.

The dissemination of this work is in 6 sections. Following this introduction, we present a brief overview of localised blast loads. In section §3 we develop the methodology of our numerical study, followed by the result and discussions in section §4. In section 5 an analytical solution for the dimensionless impulse is presented, which can determine the effectiveness of the shell to withstand the perforation of impulse due to a localised blast. Finally, in section §6 the concluding remarks of this study are presented.

2. LOCALISED BLAST LOAD

A blast wave is generated by a rapid release of energy due to the detonation of a high explosive and is a pulse with a single peak and an often diminutive time duration. In this work, the blast wave is assumed to be generated by multiple cylindrical explosives of a certain mass M_e, having the diameter D_e, the heat energy per mass of Q_e which is placed at a stand-off distance s_D, the vertical distance from the top coordinate of the target shell. This gives parameters defining the cylindrical blast source uniquely as: M_e, s_D, D_e, and Q_e.

The blast wave pressure can be truncated into the first component of its multiplicative decomposition of functions of the spatial part (load shape) and temporal part (pulse shape) [40], given in Eq. (1),

$$p^*(\theta, x, t) = P(\theta, x)p_3(t). \tag{1}$$

The Spatial distribution of blast loading $P(x,\theta)$ owes its profile to the geometry of the initial curvature of the target. For the targets of zero curvature, such as beams and plates, the suitable function is to presume as uniformly distributed over the central zone from the point of projection of the load over the target surface, while exponentially decaying over the surrounding part of the plate. For the blast source and the plates of coaxial normal from their centres, this pressure profile reads [41]:

$$p(r) = \begin{cases} 1 & 0 \le r \le r_e \\ ae^{-br} & r_e \le r \le L \end{cases}, \tag{2}$$

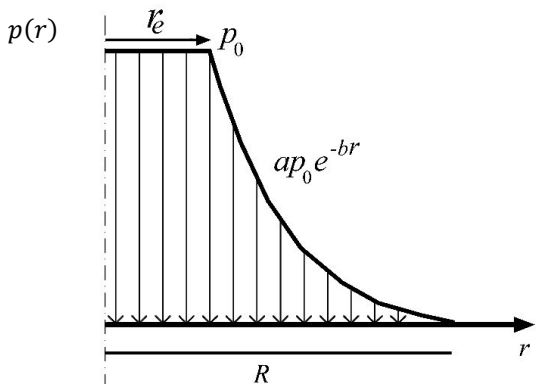

(a)

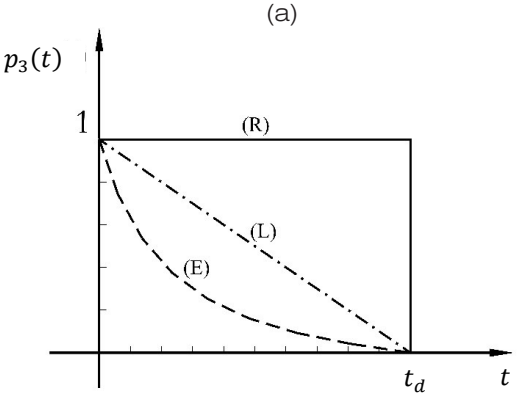

(b)

Figure 1- (a) Spatial distribution of the pulse pressure load (Load shape), (b) Temporal distribution of the load (pulse shape) Rectangular (R), Linear (L) and Exponential (E). p_0 is the maximum overpressure.

where r is the radial distance from the projection point of the charge on the target surface. This profile is depicted in Figure 1a. Various functions are proposed to describe the load pulse shape. These may include but are not limited to, the rectangular, exponential, sinusoidal, and triangularly decaying functions (Figure 1b). The former profile applies to the impulsive load

case scenarios. The exponential function relates to the blast loads generated from high explosives, in which case it may be idealised with the Friedlander equation [42]. A convenient, dimensionless form of the pulse shape is expressed in Eq. (3).

The sinusoidal pulse profile arises from the gas explosions which has a finite duration. While the elastic and perfectly plastic dynamic vibrations of the target [18], [26], [43] have a strong dependence on the pulse shape, the pulse shape influence may be eliminated through the introduction of effective pressure and impulse parameters [44].

For the blast profile given in Figure 1, the parameters that fully define the loading profile are: p_0, t_d, α, b and R_e. It should be noted that the parameter $a = e^{bR_e}$ is not an independent parameter as it links the two functions proposed for the spatial distribution of loading through ensuring the continuity of that profile.

$$p_3(t) = (1 - Xt/t_d\,)e^{-Yt}, \tag{3}$$

where X, Y are the coefficients to be determined from experimentations or numerical simulations. Eq. (3) reduces to the linear pressure profile upon the choice of $Y = 0$, or to the exponential case $p_3(t) = \exp(-Yt)$ with the choice of $X = 0$. In this work, we examine the exponential profile given by $X = 1$.

3. MATERIALS AND MODELS

The present work deals with the examination of the external, multiple blast scenarios on the generic cylindrical shell with a circular cross section. Cylindrical shells have wide industrial applications as pipes, hollow beams and columns used in buildings, aircraft fuselages, horizontal axis wind turbine pylons of the monopiles, and jacket foundations. This research is thus twofold, in the first part of which we examine the FSI in the localised blast generated from the multiple blast scenarios from two charges which may be detonated simultaneously or sequentially with a duration lag of t_l.. In the second part, we examine the effectiveness of the shell to withstand the imparted impulse. The analyses of blast circumstances lend themselves to the use of advanced techniques encompassing Fluid-Structure Interaction (FSI).

A schematic of the generic shell to be studied with the loading applied is depicted in Figure 2. The coordinates along the shell, as measured from the centre of the shell, are related to the Polar coordinates as $= Rsin\theta, y = Rcos\theta,\ s = R\theta$. For brevity in the analysis, the angular coordinate is measured from the summit node on the shell.

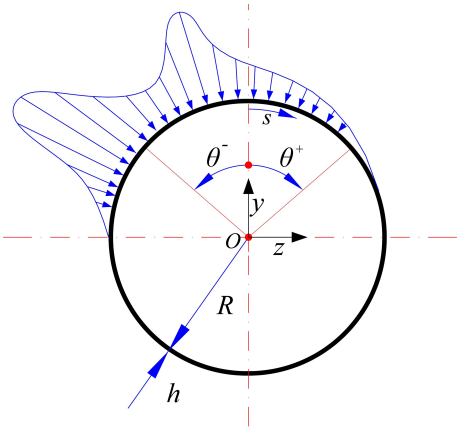

Figure 2- Cross-section of the cylindrical shell

3.1. Simulation of the blast

The physics of localised blasts, particularly those generated by multiple charges, renders the prediction of the actual dynamic solution and associated damage modes intrinsically difficult. Reliability of the FE models depends on the account for the parameters that govern the FSI, the discretisation of the FE mesh to trace the solutions for traction forces and bending moments; as well as the credibility of the input parameters utilised in the continuum mechanics equations incorporated in the FE computer programme. Unfortunately, more often than not, the coefficients are obtained empirically and vary in the literature. The plethora of values necessitates applying the consistency tests and validation of numerical models with experiments. However, the multiphysics techniques that account for the fluid compressibility in air blast, such as the multi-material arbitrary Lagrangian-Eulerian (MMALE) provide promising predictions of the blast pressure and the ensuing target deformation.[14], [27], [45].

Hence, the fluid advection and the pressure are investigated using MMALE analyses. The MMALE utilises continuum mechanics algorithms to obtain the solutions for the arbitrary motion of fluid mesh points relative to the (fixed reference) Eulerian points. In other words, a material Eulerian element may contain different material points and the mesh does not necessarily follow the motion of material points. For the problem at hand, the multi-material in the model consists of air and the explosive which occupy a fraction of the Eulerian medium. Upon contact with the detonation front, the solid material points within the unreacted explosive instantaneously convert into the gaseous products which propagate through the medium. This process is accompanied by a rapid release of energy which causes the air in front of the gaseous products to be compressed, generating a shock-front. The program incorporates the flux limiting process to capture the second-order advection which enables the transference of the state variables (temperature, pressure, velocity) to the target. At the contact interface between the fluid and structural target, the deformation and deformation gradients of the target can be determined from the conservation of momentum between the target mesh points and the explosive gaseous products.

A 3-dimensional Eulerian cuboid containing the air and explosives was set up in finite element hydrocode ABAQUS/Explicit. The schematics of the Finite Element model is drawn in Figure 3a. The Eulerian mesh was discretised with EC38R elements of 4mm length (Figure 3b). These are 8-noded, linear, multi-materials brick elements with reduced integration and hourglass control. Due to symmetry, only half of the physical space was integrated into the model with symmetry boundary conditions applied on the related segments of the boundary. The target was considered as a cylindrical shell of 50 mm radius and 250 mm half-length (500 mm full length). The target has been assumed as rigid, to capture the pressure and accordingly calculate the impulse. This is achieved by prescribing fixed boundary conditions to the Eulerian elements at the contact interface, The Eulerian medium hence had a size of 400 mm×250 mm×200mm. The transmission boundaries on the other faces of the medium were prescribed with free outflow boundary conditions as seen in Figure 3.

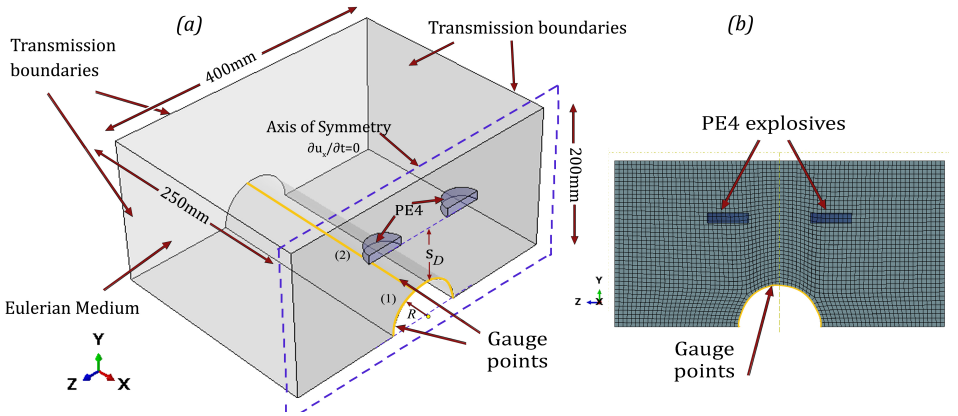

Figure 3- (a) Schematics of the MMALE model, (b) FE mesh

For the air blast loading, the space was initially filled with air, modelled as an ideal gas with the following equation of state:

$$P_a = (C_p - C_v)\rho_a T. \tag{4}$$

where P_a is the air gas pressure, $C_p = 1.005\ \mathrm{kJ/KgK}$ and $C_v = 0.7176\ \mathrm{kJ/KgK}$ are the specific heat parameters at constant pressure and constant volume, respectively, $\rho_a = 1.228\ \mathrm{kg/m^3}$ is the air density and T is the gas temperature the reference value of which is 289 K [46].

The Eulerian medium housed two cylindrical PE4 explosives of $h_e = 12mm$ height and $D_e = 50mm$ diameter mounted at either 50 mm or 75 mm stand-off distances above the top surface of the shell, in separate analyses. The mass of each charge may be calculated as $M_e = \rho_e \frac{\pi D_e^2}{4} h_e = 37.72g$. These explosives were either detonated simultaneously or sequentially. In the latter case, the charge on the right hand of the middle axis was detonated $50\mu s$ later than one on the left. For the air blast explosion, the explosive was modelled by Jones -Wilkins-Lee Equation of state as:

$$P_e = A\left(1 - \frac{\omega\rho}{R_1\rho_0}\right)e^{-R_1\frac{\rho_e}{\rho' p}} + B\left(1 - \frac{\omega\rho}{R_2\rho_0}\right)e^{-R_2\frac{\rho_e}{\rho' p}} + \frac{\omega\rho^2}{\rho_0}E_{m0}. \tag{5}$$

where $\rho' p$ is the density of the explosive product, ρ_e is the density of the explosive at the beginning of the process, A, B, R_1, R_2, and ω are the material constants [46], and E_{m0} is the specific internal energy, as presented in Table 1. The detonation is triggered from the centre of the explosive mass. The value of specific heat energy Q_e for PE4 is taken from Ref [47].

Table 1- Material properties of air and the plastic explosive (after Ref [48]

Material	ρ_e [kg. m^{-3}]	**Detonation. Wave speed** v [m/s]	A [GPa]	B[GPa]	R_1	R_2	ω	E_m [kJ/kg]	**Pre-det. bulk modulus**
PE-4	1601	8193	6.0977 ×10^{11}	1.295 ×10^{10}	4.5	1.4	0.25	6.057 ×10^{6}	0

Air	ρ_a [kg/m^3]	μ_k [$\mu Pa.s$]	P_a (Pa)	E_0	Specific heat constant (at high temperature) $C_p - C_v$ [Jkg^{-1}K^{-1}]
	1.293	18.27	101325	2.5×10^{-4}	287

For each test, the inflow of pressure was quantified across the gauge points in circumferential directions as well as in the axial direction of the shell. The blast pressure decays from the centre of the points of projection along both the circumferential and axial distances.

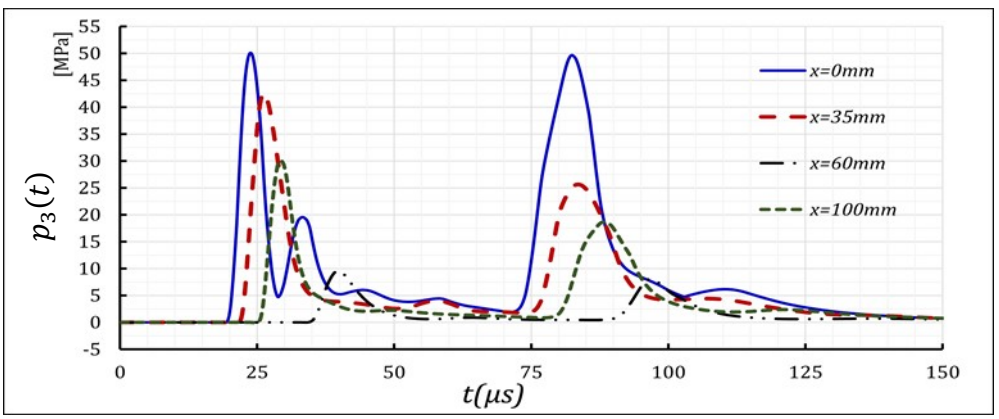

Figure 4- pressure-time histories of the sequential detonations for 75mm stand-off, at different locations across the shell.

4. RESULTS AND DISCUSSIONS

The evolution of the blast overpressure with time is plotted in Figure 4 for the sequential loading case. The two highest summits of the overpressure, occurring at 25μs and 85μs, correspond to the blast loads at interfaces to the left and right of the shell, respectively. In the case of simultaneous blasts, a zone of high pressure emanates from the detonation of the two charges covering an elliptical area, which then expands and propagates in an orthogonal direction to the plane passing through the axis connecting the centres of explosives and perpendicular to the plane of the circular base of each charge i.e. the bisector plane of the axis. When the two charges, arranged in the horizontal direction, detonate simultaneously they typically generate two shock fronts, the first peak is the offspring of the constructive superposition which travels to either side of the normal to the virtual axis connecting the two charges, while the other is attributed to the outward propagation of the gaseous products of each explosive which impinges upon the target underneath.

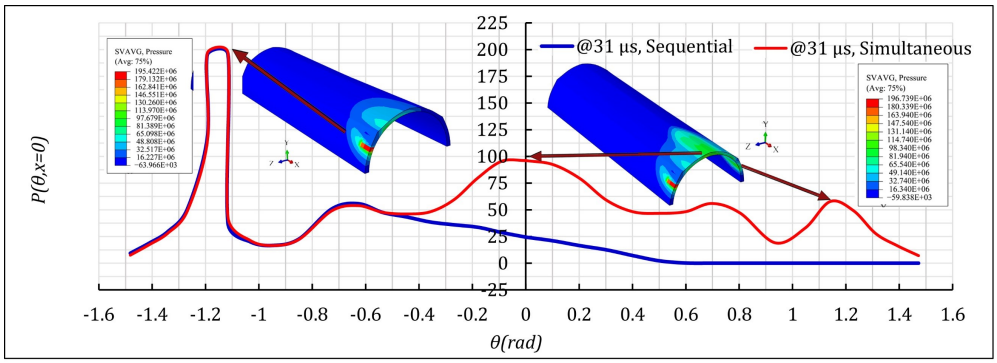

(a)

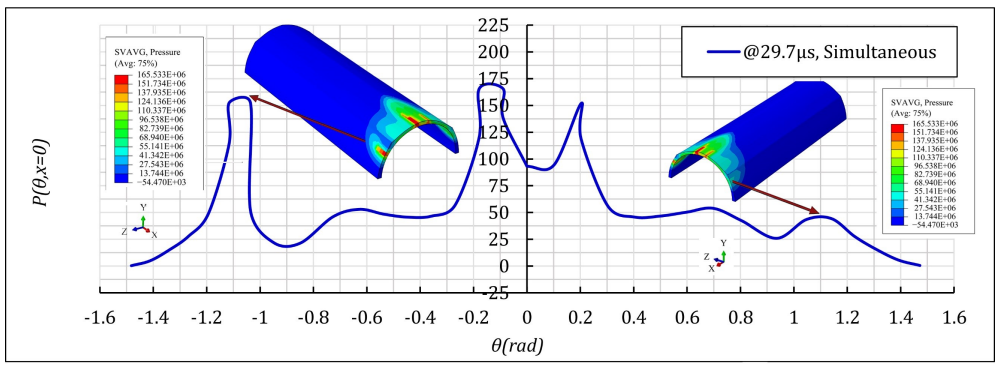

(b)

Figure 5- Pressure profile of the simultaneous and sequential detonations for 75mm stand-off. (a) comparison of the simultaneous and sequential loads. (b) peak pressure distribution across the shell

The pressure profile of the sequential and simultaneous blasts are presented in Figure 5-Figure 6. An interesting feature of the blast scenarios is the coincidence of the two blast profiles from the simultaneous and sequential blasts. Due to the geometry of the shell and the proximity of blasts, the gauge points of arc (1) in Figure 3, which are positioned over 30 mm the left arc length s measured from the top line of the shell (line (2)), are impervious to the blast pressure generated on the right side of that line.

In the sequential case of 75mm stand-off, the blast pressure arrives at 20μs from the onset of detonation. The subsequent blast pressure reaches the target 65μs later, at 31.42mm arc length to the left of the line (2). Such coordinates are the closest to the blast centre of detonation. The peak blast pressure, however, occurs at the gauge points underneath each charge, which lie on the 63mm arc length to the left of the line (2). This elevated pressure occurs at 31μs with a sharp rise in the profile. In the subsequent blast loading, a rather symmetric profile to the previous one occurs at relatively equal arc length, but to the right of the shell.

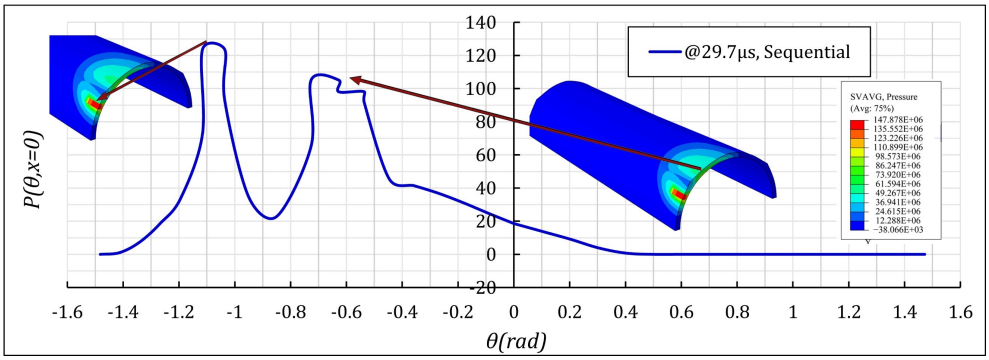

(a)

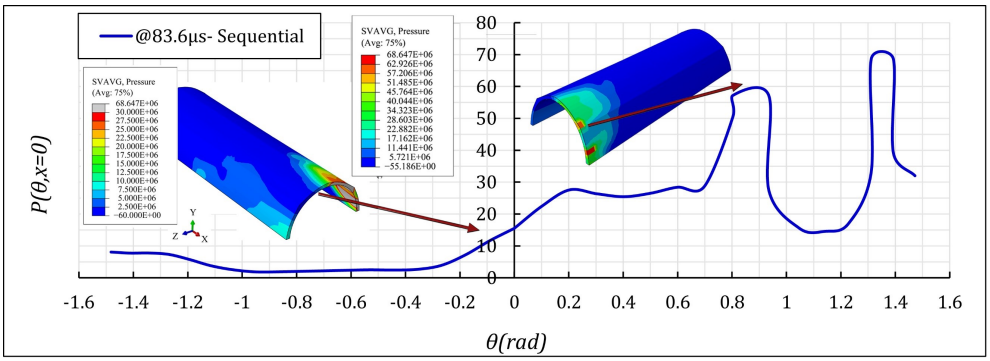

(b)

Figure 6- Distribution of the pressure across the circumference of the shell, (a) due to the detonation of the first charge, (b) due to the detonation of the second charge. The unit of the ordinates is MPa

Comparing now Figure 5 with Figure 7, the position of the peak pressure on the shell moves towards the point of projection of the charge on the shell with the increase in the stand-off. The simultaneous blast, however, generates a more severe pressure profile to the right side of the shell. In such a scenario, the target experiences a blast with two peaks along the surface, the first due to the superposition of the two blasts which impacts the top surface of the shell, while the other lies at 1.1 radians (63mm along the arc length) to the right and left of the shell, which pertain to the gauge points somewhat underneath the cylindrical charges [28].

The impulse density of the blast is calculated and plotted in Figure 8. The impulse density is measured as the impulse per unit area and is a function of the pressure load over time corresponding to the gauge points of the chosen surface.

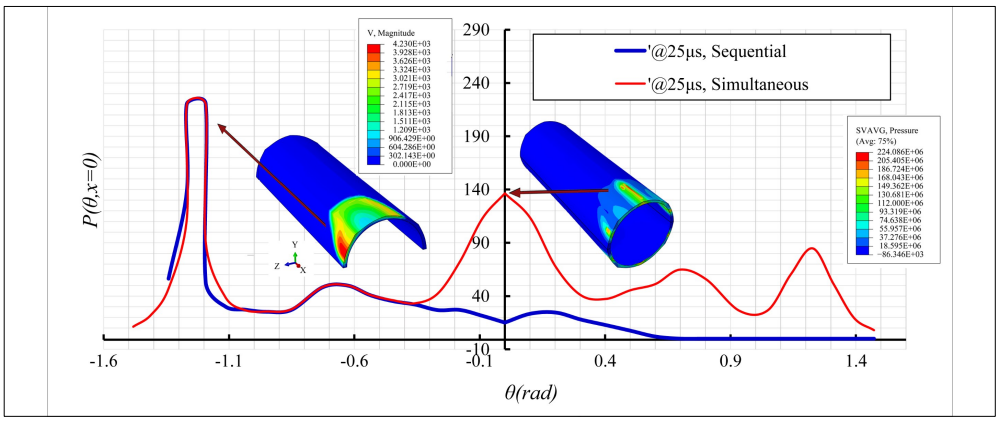

Figure 7- pressure distribution from the simultaneous and sequential blasts at 50mm stand-off

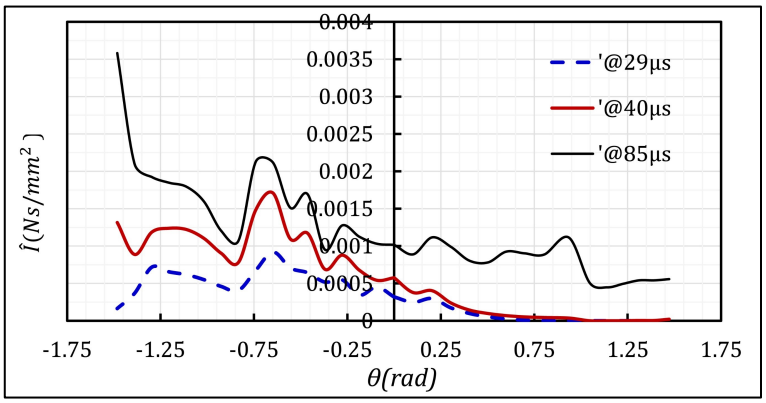

(a)

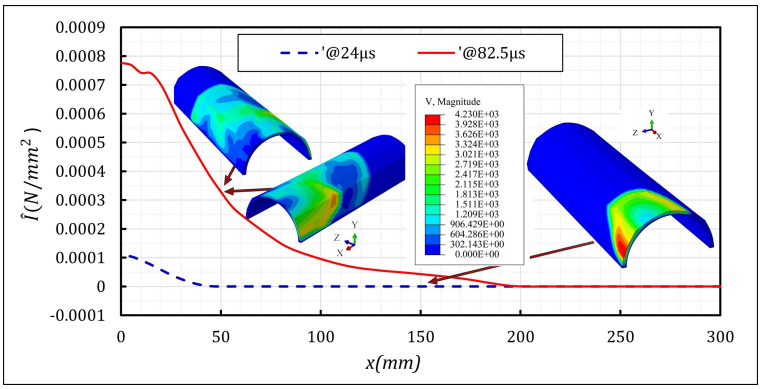

(b)

Figure 8- Impulse density of the 50mm stand-off- simultaneous loading, (a) across θ, (b) across the axial length x.

Concerning the pressure profile in the axial direction, both pressures registered at the gauge points along the top of the shell, as well as those along the along the axial line (2) starting from the gauge points with the peak pressure were monitored. To investigate the dependence of the pressure in the axial direction on the generalized coordinate θ, the pressure profile along an arbitrarily chosen third axial path was also captured. Clearly, the pressure profile across those paths rendered similar profile, hence the spatial components of the blast pressure have independent density functions, i.e., the blast pressure $P(\theta, x) = p_1(\theta)p_2(x)$ may be truncated into the single term of its multiplicative decomposition.

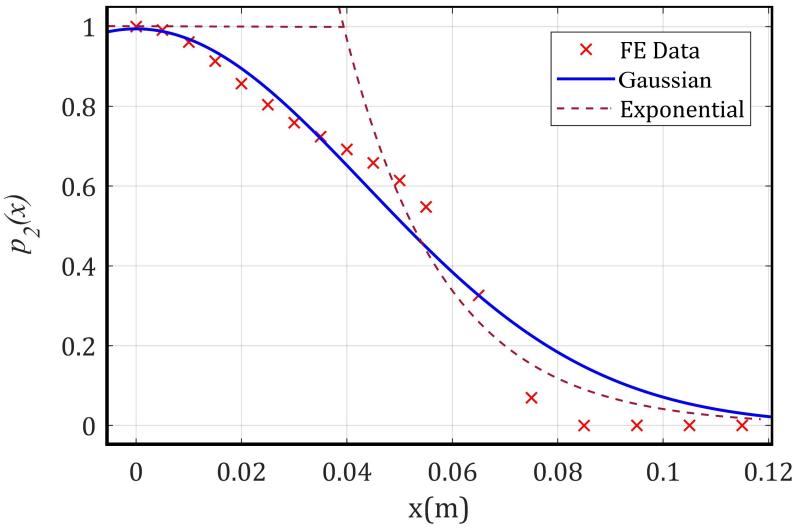

(a)

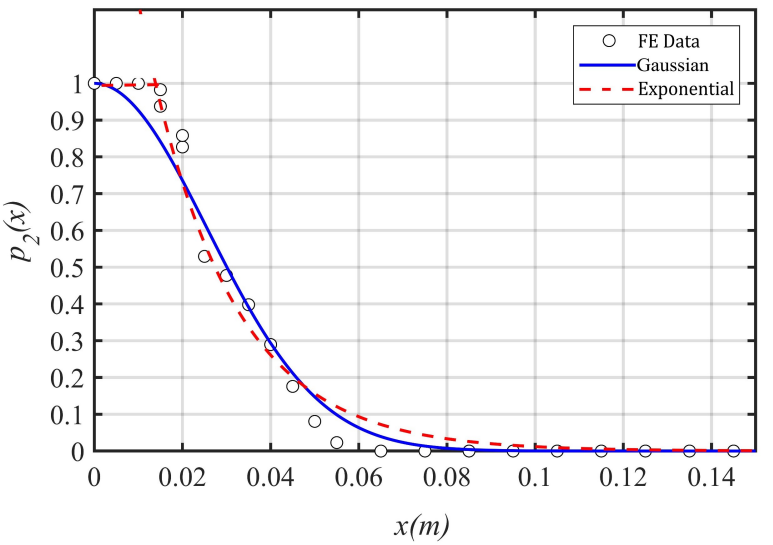

(b)

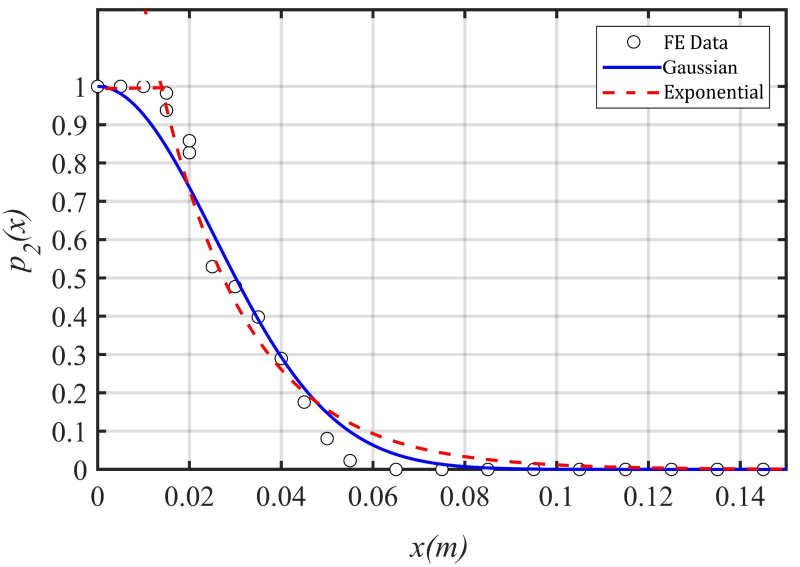

(c)

Figure 9- Validation of the FE data with the empirical models. (a) Prediction of the pressure profile across θ using the Gaussian distribution with two terms. (b) the load shape models in axial direction using the uniform-exponential and the Gaussian density function for 75mm stand-off, (c) predicted load shape models in the axial direction with 50mm stand-off.

The normalised load shape functions may be determined empirically by performing the curve fitting of the pressure registered at the gauge points in the circumferential and axial directions of the shell. The curve fitting was carried out with the MATLAB built-in Curve fitting capability. We depict the results of the analysis in Figure 9. Although the commonly accepted load shape of the blast (with x replacing r in Eq. (2) still predicts the variation of the pressure along the axial distance favourably with a high coefficient of confidence ($R^2 = 0.93$), an alternative is to prescribe the bell curved, Gaussian distribution function to model the load shape, as expressed in Eq. (6). The Gaussian distribution function has a mean of 0 and a low standard deviation. This function is more pertinent to the higher stand-off values. The parameters of each load shape model are summarized in Table 2.

$$p_2(x) = ae^{-\left(\frac{x-b}{\sigma_{dv}}\right)^2}. \tag{6}$$

Table 2- Parameters of the modified exponential (E(x)) and the Gaussian (G(x)) distribution functions, defined in Eq. (2) and Eq. (6), respectively, the spatial distribution of the pressure across the length of the shell

Blast Scenario	**Pressure function**	**Stand-off Distance**	$a[1]$	$b[m]$	$\sigma_{dv}[m]$	$r_e[mm]$
Simultaneous	G(x)	50	1	0	0.03613	-
	E(x)		2.0434	51.43	-	15
Sequential	G(x)	50	1	0	0.0284	-
	E(x)		2.624	76.31	-	15
Simultaneous	G(x)	75	1	0	0.0614	-
	E(x)		7.93	52.6	-	40
Sequential	G(x)	75		0	0.0286	-
	E(x)		1	61.99	-	20

Nevertheless, with the increase in charge diameter of the proximal blasts, the uniform-exponential model (Eq. (2)) yields an accurate prediction of the load shape [19]. The decision to classify the blast source as proximal or distal may be determined by the use of Hopkinson-Cranz scaled distance value or graphs of stand-off to charge diameters available in [4], [27], [45]. Concerning the uniform-exponential model, the radius of the portion varies from 15mm to 40mm with a 25 mm stand-off increase. For the load shape across the generalised coordinate θ, the corresponding Gaussian distribution function is described with two terms:

$$p_1(\theta) = a\exp\left(\left(\frac{\theta-b}{\sigma_{dv1}}\right)^2\right) + c\exp\left(\left(\frac{\theta-d}{\sigma_{dv2}}\right)^2\right), \tag{7}$$

where $\sigma_{dv1}, \sigma_{dv2}$ are the standard deviations, a, b, c, d are the constants to be found through the curve fitting models.

We now investigate the shell response to different pressure profiles by applying the load on the flexible cylinder using the uncoupled analysis. To this end, the load shape was prescribed as a set of data points corresponding to the points at each section across the shell (with θ varying along the circumference). The surface pressure of each coordinate was generated as the product of the pressure registered by the gauge points in the circumferential path with axial pressure profile defined with the Gaussian distribution function. The flexible shell had identical dimensions to the rigid one, but with a shell thickness of 2mm. The shell was made of visco-plastic Mild Steel, with a Young modulus of $E = 200\text{GPa}$, Poisson's ratio of $\nu = 0.3$, static yield stress of $\sigma_0 = 325MPa$.

The plots of the stress-strain constitutive relation of this material, denoted therein as MS4, may be found in [14] and [49]. The Cowper-Symonds equation was used to describe the visco-plasticity (strain rate sensitivity) of the material. The shell was embedded 25mm into two clamps of outer radiuses of 75mm and 100mm, respectively, with a prescribed penalty friction coefficient of 0.3 to model the tangential contact behaviour between the interfaces. The model was prescribed with symmetric boundary conditions in the same fashion as the rigid one. The model was discretized with a uniform mesh of 4mm S4R conventional doubly curved shell elements with 5 Simpson points of integration through the thickness and reduced integration hourglass control. The clamps were fixed in space and modelled as rigid cylinders whose mesh may be chosen as coarse to preserve computational time at no loss of accuracy.

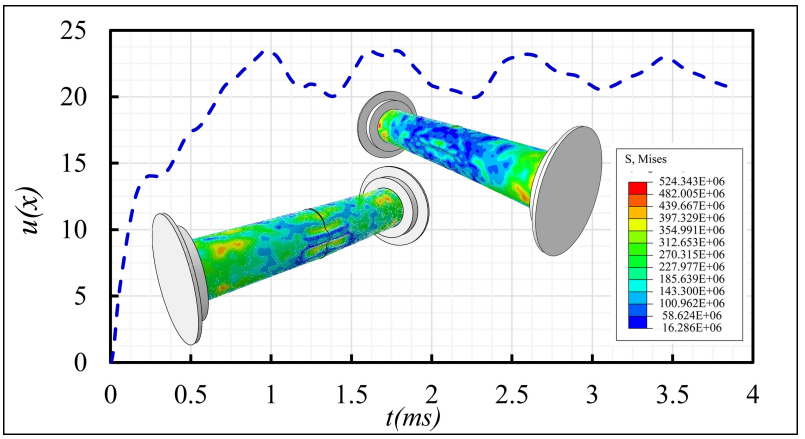
25
20
15
10
5
0
u(x)
0
0.5
1
1.5
2
2.5
3
3.5
4
t(ms)
S, Mises
524.343E+06
482.005E+06
439.667E+06
397.329E+06
354.991E+06
312.653E+06
270.315E+06
227.977E+06
185.639E+06
143.300E+06
100.962E+06
58.624E+06
16.286E+06

(a)

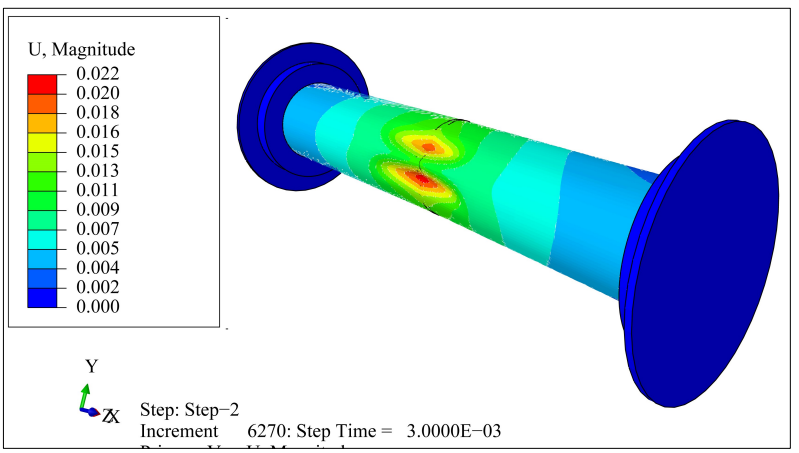
U, Magnitude
0.022
0.020
0.018
0.016
0.015
0.013
0.011
0.009
0.007
0.005
0.004
0.002
0.000
Y
Z
X
Step: Step−2
Increment 6270: Step Time = 3.0000E−03

(b)

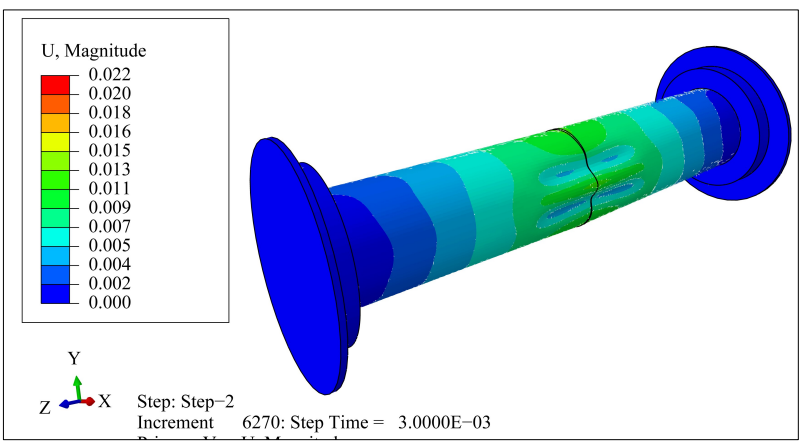
U, Magnitude
0.022
0.020
0.018
0.016
0.015
0.013
0.011
0.009
0.007
0.005
0.004
0.002
0.000
Y
Z
X
Step: Step−2
Increment 6270: Step Time = 3.0000E−03

(c)

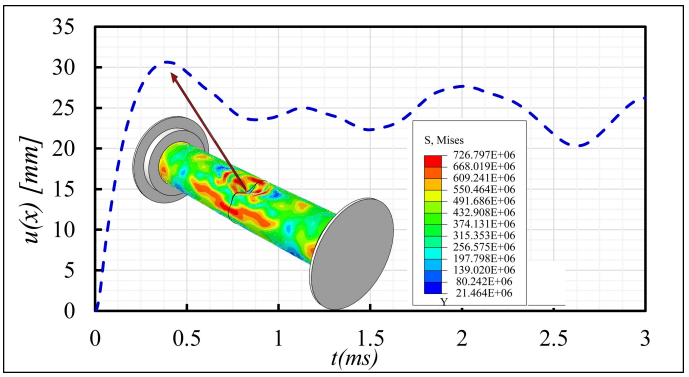

(d)

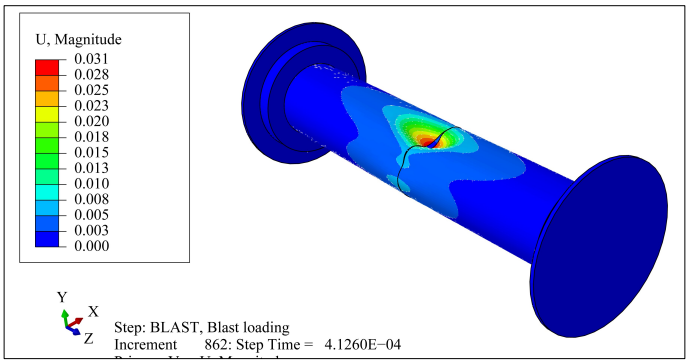

(e)

Figure 10- (a) Maximum translational transient deformation of the shell due to the sequential blast with 75mm stand-off (b), (c) schematics of the permanent deformation of the shell with bulging shown to the left and right side of the shell, respectively. (d) Maximum transient deformation of the shell due to simultaneous blasts. (e) schematics of the shell maximum deformation. The units of the legends are SI units, while the unit of the ordinate of (a) is mm

In Figure 10 we compare the results for the 75mm stand-off for the sequential and simultaneous blasts. The difference in the response of the shell to each loading case is distinguishable. The sequential blast generates two bulging curves at either side of the shell, with the first wave transmission penetrating further/ inducing a deeper bulge in the shell than the latter one. The simultaneous blast impacts a single, deep bulge on top of the shell, induced by the superimposed waves, together with a smaller bulge occurring on the left side, underneath the charge on that side.

Concerning the sequential blasts, the recorded maximum permanent deformation was 24.9mm pertaining to the bulge with negative angular coordinates corresponding to the region of the first peak in Figure 6a ($-0.8 \leq \theta \leq -0.6$) which was 6.3% larger than the one at the projection point of the charge ($\theta \cong -1.1$). The two permanent deformations in the bulges that appeared on the right side of the shell (positive θ) were on average 44.7% smaller than the maximum deformation on the left side of line (2). The reason is attributed to the higher peak pressures registered with the negative angular coordinates.

5. IMPULSIVE LOADING

The total impulse imparted onto the outer surface of a cylindrical shell of fixed radius R is, as presented in Eq. (8), the functional of the pressure distribution over the generalized coordinates x, θ and time t over a finite space and time. The impulse is measured from the centre of the projection to the characteristic distance L measured from the centre of the shell.

$$I(u) = 2R \int_0^u \int_{\theta_1}^{\theta_n} \int_0^{t_d} P(\theta, x) p_3(t) dt d\theta dx \,, \tag{8}$$

where $\theta_1 = 0$ and $\theta_n = \pi$. Assuming the impulse imparted over the defining $\lambda_0 = l_e/L$ and $\lambda = u/L$, the pressure distribution concerning the angular coordinate θ may be evaluated numerically by discretizing the surface into a finite number of nodes, giving:

$$I(u) = 2R \sum_{i=1}^{n} p_1(\theta_i) \int_0^u \int_0^{t_d} p_2(x) p_3(t) dt dx \,. \tag{9}$$

Substituting Eq. (2) into Eq. (9) and noting that $f(\theta) = 2R \sum_{i=1}^{n} p_1(\theta_i)$ yields:

$$I(\lambda) = \begin{cases} \frac{P_0(Yt_d + e^{-Yt_d} - 1)(\lambda_0 L) f(\theta)}{t_d Y^2} & \lambda < \lambda_0 \\ \frac{P_0(Yt_d + e^{-Yt_d} - 1)}{t_d Y^2 b} [1 - \exp(-(\lambda - \lambda_0) bL)] f(\theta) & \lambda \geq \lambda_0 \end{cases}, \tag{10}$$

where P_0 is the maximum overpressure. The total impulse that the charge could potentially impart to the target would thus be given by:

$$I(\infty) = \lim_{\lambda \to \infty} \{I(\lambda)\} = \frac{P_0(Yt_d + e^{-Yt_d} - 1)}{t_d Y^2 b} f(\theta). \tag{11}$$

Thus, a non-dimensional impulse, $\bar{I}$, can be defined as the quotient of the impulse imparted to a target over the total impulse that the blast can generate:

$$\bar{I} = \frac{I(\lambda)}{I(\infty)} = \begin{cases} \lambda bL & \lambda < \lambda_0 \\ 1 - \exp\big((\lambda_0 - \lambda) bL\big) & \lambda \geq \lambda_0 \end{cases}. \tag{12}$$

For the Gaussian distribution profile, the impulse imparted by the charge, over the finite region over the finite region λ_0 to λ reads:

$$I\,(\lambda) = \frac{(Yt_d + e^{-Yt_d} - 1) a P_0 \sigma_{dv} \sqrt{\pi}}{2 t_d Y^2} \left[\operatorname{erf}\left(\frac{\lambda L - \mu}{\sigma_{dv}}\right) - \operatorname{erf}\left(\frac{\lambda_0 L - \mu}{\sigma_{dv}}\right) \right] f(\theta). \tag{13}$$

In the same fashion, the total impulse generated by the charge can be expressed as:

$$I(\infty) = \lim_{\lambda \to \infty} \{I(\lambda)\} = \frac{(1 + Yt_d - e^{-Yt_d}) a P_0 \sigma_{dv} \sqrt{\pi}}{2 t_d Y^2} \left[1 - \operatorname{erf}\left(\frac{\lambda_0 L - \mu}{\sigma_{dv}}\right) \right] f(\theta) \tag{14}$$

with $\mu = 0$ here. The dimensionless impulse is then the quotient of the two impulses expressed as:

$$\bar{I} = \frac{I(\lambda)}{I(\infty)} = \frac{\left[\text{erf}\left(\frac{\lambda L-\mu}{\sigma_{dv}}\right)-\text{erf}\left(\frac{\lambda_0 L-\mu}{\sigma_{dv}}\right)\right]}{\left[1-\text{erf}\left(\frac{\lambda_0 L-\mu}{\sigma_{dv}}\right)\right]}, \tag{15}$$

where

$$f(\theta) = 2R\sum_{i=1}^{n} p_1(\theta_i) \tag{16}$$

The denominator of Eq. (15) approaches unity when $\lambda_0 \to 0$ and $\mu = 0$, i.e. the cases examined in the previous section. Notably, when using the exponential distribution expressed in Eq. (2), the dimensionless impulse assumes the form [27]:

$$\bar{I} = \frac{I(\lambda)}{I(\infty)} = \begin{cases} \frac{(\lambda_0 L)^2}{2+2\lambda_0 Lb+(\lambda_0 Lb)^2} & \lambda < \lambda_0 \\ 1 - \frac{2e^{-Lb(\lambda-\lambda_0)}[1+\lambda Lb]}{2+2\lambda_0 Lb+(\lambda_0 Lb)^2} & \lambda \geq \lambda_0 \end{cases} \tag{17}$$

Eqs. (15) and (17) indicate the effectiveness of the target to dissipate the impulse being imparted upon it, relative to the total target perforation impulse, referred to as the rupture impulse or impulse threshold. The decay parameter b depends on the stand-off distance and can be determined empirically as done in [27] with a good estimate as:

$$b = \frac{2.528}{D_e}\left(\frac{s_D}{D_e}\right)^{-0.711} \tag{18}$$

As most localised blast scenarios correspond to $60 \leq b \leq 150$, of which the corresponding standard deviation varies within the range of $0 < \sigma_{dv} < 0.1$, given the finite region of $0 < \lambda < 0.5$, it transpires that the charge becomes 95% efficient in delivering the total impulse. The charge can deliver the total impulse $\bar{I} = 1$ when the extent of the pressure exceeds half the characteristic length of the target ($\lambda \geq 0.5$).

The interaction surface of dimensionless impulse against stand-off and λ (Figure 11) demonstrates that for the blast loads generated by the same mass of explosive, the cylindrical charges with small diameter and larger heights attribute more threatening blast scenarios than those with a high charge diameter but lower charge heights. This is due to the nature of the detonation waves in a cylindrical explosive which propagates in the direction of its height. The pressure wave emanated from the explosive products of larger height/diameter ratios would therefore concentrate on the centre of their projection on the target, imparting more energy locally, thus rendering a higher value of surface traction, leading to a more localised, penetrating effect. For example, within the finite region of $0 < \lambda < 0.5$, the overpressures of the material mesh points generated from the proximal blast have a less scattered distribution from their mean, generating a potentially perforating impulse. Finally, the variation of the dimensionless impulse of the distal charges ($s_d > 185mm$) over the characteristic length of the blast is smooth.

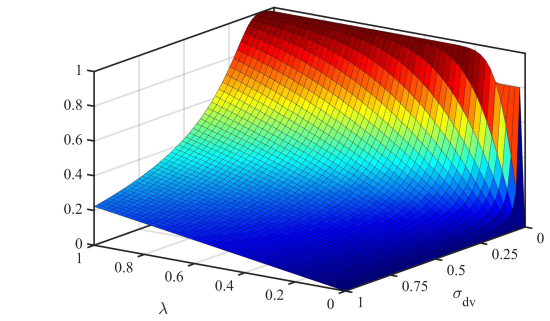

(a)

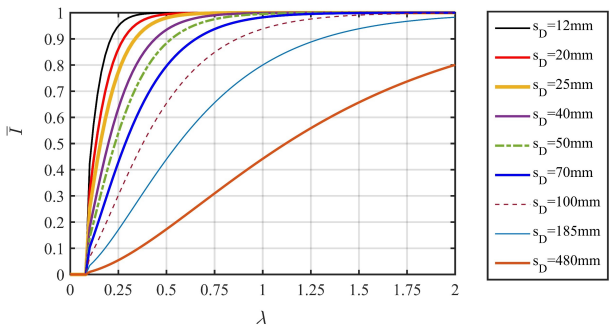

(b)

Figure 11- (a) interaction surface of the dimensionless impulse $\bar{I}$ with Gaussian distribution load shape, (b) plots of $\bar{I}$ with uniform-exponential load shape at various stand-off distances

6. CONCLUDING REMARKS

This work deals with the dynamic response of cylindrical shells of circular cross section due to multiple blasts. The FSI phenomena related to the interaction of gaseous products of detonated charges of multiple blast scenarios and air are considered. The charges are detonated one simultaneously and once sequentially. The effect of FSI due to the air blast of two identical charges, which detonated either simultaneously or sequentially, was investigated on the dynamic response of the cylindrical shell. Both types of detonations led to a similar pressure profile with negative angular coordinate θ, suggesting this side was the blind spot for the charge to the other side of the shell.

Both shells experienced a global mode deformation as well as the local modes which induced bulging at the midspan of the shell. However, in the simultaneous blast scenario, an elliptical zone of high pressure resulting from to the constructive interference/superposition of the two waves projects onto the shell. The shell subjected to such a zone experienced a high bulging in its central zone with a symmetric profile. In contrast, the sequential charge induced two bulging regions on either side of the shell with respect to the top line (2). The maximum deformation of the shell due to such loading at 75mm stand-off pertained to the left side of this line. The two bulging on this side were deeper than those occurred on the right side.

The profile of the pressure varied exponentially from the centre of projection along the length of the shell to which either the Gaussian model or the uniform-exponential models can be accurately regressed in order to predict the pressure registered at each coordinate. The pressure profile in angular direction was inherently complex and the high-order Gaussian distributions was used. The corresponding impulse density had a sharp then a smooth degradation with the increase in θ. In the axial direction, the impulse density attributes to a simpler pressure profile which varies exponentially the further away from the centre of blast.

The non-dimensional impulse was compared for each investigated load shape and revealed that the proximal charges are capable of impinging the total load generated by the charge with a probability exceeding 80%.

7. FUNDING

The authors received no financial support for the research, authorship or publication of this paper.

NOMENCLATURE

Latin Upper and Lower Case

L	Shell characteristic half lengths, [L]
$\mathrm{C_p}$	Ideal gas specific heat at constant pressure, $[\mathrm{L^2T^{-2}K^{-1}}]$
$\mathrm{C_v}$	Ideal gas specific heat at constant volume, $[\mathrm{L^2T^{-2}K^{-1}}]$
D_e	Charge diameter, [L]
E	Young's modulus, $[\mathrm{ML^{-1}T^{-2}}]$
$\hat{I}$	Impulse density, $[\mathrm{ML^{-1}T^{-1}}]$
I	Impulse transmitted to the target, $[\mathrm{MLT^{-1}}]$
$\bar{I}$	Non-dimensional impulse, [1]
M_e	Mass of explosive, [M]
P_0	Maximum overpressure, $[\mathrm{ML^{-1}T^{-2}}]$
$P(x,\theta)$	Load shape of the blast, $[\mathrm{ML^{-1}T^{-2}}]$
Q_e	Specific Heat Energy, $[\mathrm{L^2T^{-2}}]$
R	Shell radius, [L]
Y	Pulse shape decay constant, $[\mathrm{T^{-1}}]$
a	Load shape explosive constant, [1]
b	Load shape explosive decay constant, $[\mathrm{L^{-1}}]$
h	Shell thickness, [L]
h_e	Charge height, [L]
$p^*(\theta,x,t)$	Overpressure Load, $[\mathrm{ML^{-1}T^{-2}}]$
$p_2(x)$	Dimensionless axial component of the load shape direction, [1]
$p_1(\theta)$	Dimensionless angular component of the load shape direction, [1]
r	Generalized radial coordinates, [L]
r_e	Radius of the centrally loaded target in the axial direction, [L]

s_D	Stand-off distance, [L]
t_d	Duration of the blast load, [T]

Greek Lower case

ρ_p	Shell mass density, [ML^{-3}]
ρ_e	Explosive density, [ML^{-3}]
ρ_a	Fluid (air) density, [ML^{-3}]
σ_{dv}	Standard deviation, [L^{-1}]
ν	Poisson's ratio
a	Load shape explosive constant, [1]
μ_k	Dynamic viscosity of air, [$ML^{-1}T^{-1}$]
σ_0	Material static yield stress, [$ML^{-1}T^{-2}$]
σ_{UT}	Ultimate static tensile stress, [$ML^{-1}T^{-2}$]

REFERENCES

[1] N. Kambouchev, R. Radovitzky, and L. Noels, "Fluid–Structure Interaction Effects in the Dynamic Response of Free-Standing Plates to Uniform Shock Loading," J. Appl. Mech., vol. 74, no. 5, p. 1042, 2007.

[2] N. Kambouchev, L. Noels, and R. Radovitzky, "Nonlinear compressibility effects in fluid-structure interaction and their implications on the air-blast loading of structures," J. Appl. Phys., vol. 100, no. 6, pp. 063519 1–11, 2006.

[3] G. I. Taylor, "The pressure and Impulse of Submarine Explosion Waves on Plates," in The scientific papers of Sir Geoffrey Ingram Taylor: Vol 3 Aerodynamics and the Mechanics of Projectiles and Explosions, vol. III, no. 4, G. K. . Batchelor, C. F. . Sharman, J. W. . Maccoll, R. M. . Davies, H. ; Jones, and P. G. . Saffman, Eds. Cambridge, UK: Cambridge University Press, 2011, p. 590.

[4] DOD., Unified Facilities Criteria (UFC): Structures to Resist the Effects of Accidental Explosions (UFC 3-340-02), no. December. Washington DC.: Department of Defence, 2008.

[5] A. Neuberger, S. Peles, and D. Rittel, "Springback of circular clamped armor steel plates subjected to spherical air-blast loading," Int. J. Impact Eng., vol. 36, no. 1, pp. 53–60, 2009.

[6] M. D. Olson, G. N. Nurick, and J. R. Fagnan, "Deformation and rupture of blast loaded square plates—predictions and experiments," Int. J. Impact Eng., vol. 13, no. 2, pp. 279–291, 1993.

[7] G. LeBlanc, M. Adoum, and V. Lapoujade, "External blast load on structures – Empirical approach," 5th Eur. LS-DYNA Users Conf., no. 2, 2005.

[8] I. Sochet, D. Gardebas, S. Calderara, Y. Marchal, and B. Longuet, "Blast Wave Parameters for Spherical Explosives Detonation in Free Air," Open J. Saf. Sci. Technol., vol. 01, no. 02, pp. 31–42, 2011.

[9] G. S. Langdon, S. C. K. Yuen, and G. N. Nurick, "Experimental and numerical studies on the response of quadrangular stiffened plates. Part II: Localised blast loading," Int. J. Impact Eng., vol. 31, no. 1, pp. 85–111, 2005.

[10] S. C. K. Yuen and G. N. Nurick, "Experimental and numerical studies on the response of quadrangular stiffened plates. Part I: Subjected to uniform blast load," Int. J. Impact Eng., vol. 31, no. 1, pp. 55–83, 2005.
[11] S. C. K. Yuen and G. N. Nurick, "Experimental and numerical studies on the response of quadrangular stiffened plates. Part I: Subjected to uniform blast load," Int. J. Impact Eng., vol. 31, no. 1, pp. 55–83, 2005.
[12] V. Aune, E. Fagerholt, K. O. Hauge, M. Langseth, and T. Børvik, "Experimental study on the response of thin aluminium and steel plates subjected to airblast loading," Int. J. Impact Eng., vol. 90, pp. 106–121, 2016.
[13] T. Børvik, O. S. Hopperstad, and T. Berstad, "On the influence of stress triaxiality and strain rate on the behaviour of a structural steel. Part II. Numerical study," Eur. J. Mech. A/Solids, vol. 22, no. 1, pp. 15–32, 2003.
[14] N. Mehreganian, L. A. Louca, G. S. Langdon, R. J. Curry, and N. Abdul-Karim, "The response of mild steel and armour steel plates to localised air-blast loading-comparison of numerical modelling techniques," Int. J. Impact Eng., vol. 115, no. January, pp. 81–93, 2018.
[15] V. Aune, G. Valsamos, F. Casadei, M. Larcher, M. Langseth, and T. Børvik, "Numerical study on the structural response of blast-loaded thin aluminium and steel plates," Int. J. Impact Eng., vol. 99, pp. 131–144, 2017.
[16] T. Børvik, A. G. Hanssen, M. Langseth, and L. Olovsson, "Response of structures to planar blast loads - A finite element engineering approach," Comput. Struct., vol. 87, no. 9–10, pp. 507–520, 2009.
[17] K. Micallef, A. S. Fallah, P. T. Curtis, and L. A. Louca, "On the dynamic plastic response of steel membranes subjected to localised blast loading," Int. J. Impact Eng., vol. 89, pp. 25–37, 2016.
[18] N. Mehreganian, M. Toolabi, Y. A. Zhuk, F. Etminan Moghadam, L. A. Louca, and A. S. Fallah, "Dynamics of pulse-loaded circular Föppl-von Kármán thin plates- Analytical and numerical studies," J. Sound Vib., vol. 513, p. 116413, 2021.
[19] N. Mehreganian, A. S. Fallah, and L. A. Louca, "Plastic dynamic response of simply supported thick square plates subject to localised blast loading," Int. J. Impact Eng., vol. 126, no. December 2018, pp. 85–100, 2019.
[20] N. Jones, "Dynamic inelastic response of strain rate sensitive ductile plates due to large impact, dynamic pressure and explosive loadings," Int. J. Impact Eng., vol. 74, pp. 3–15, 2014.
[21] N. Jones, Structural Impact. Cambridge: Cambridge University Press, 1989.
[22] Q. M. Li and H. Meng, "Pressure-impulse diagram for blast loads based on dimensional analysis and single-degree-of-freedom model," J. Eng. Mech., vol. 128, no. 1, pp. 87–92, 2002,
[23] A. S. Fallah and L. A. Louca, "Pressure-impulse diagrams for elastic-plastic-hardening and softening single-degree-of-freedom models subjected to blast loading," Int. J. Impact Eng., vol. 34, no. 4, pp. 823–842, 2007.
[24] N. Mehreganian, A. S Fallah, and L. A. Louca, "Inelastic dynamic response of square membranes subjected to localised blast loading," Int. J. Mech. Sci., vol. 148, no. November, pp. 578–595, 2018.

[25] N. Mehreganian, A. S. S. Fallah, and L. A. A. Louca, "Dynamic Performance of Simply Supported Rigid-Plastic Square Plates Subject to Localized Blast Loading," J. Eng. Mech., vol. 140, no. 1, pp. 159–171, 2018.

[26] N. Mehreganian, A. S. S. Fallah, and L. A. A. Louca, "Nonlinear dynamics of locally pulse loaded square Föppl–von Kármán thin plates," Int. J. Mech. Sci., vol. 163, no. February, 2019.

[27] N. Mehreganian, A. S. S. Fallah, G. K. K. Boiger, and L. A. A. Louca, "Response of Armour Steel Square Plates To Localised Air Blast Load- a Dimensional Analysis," Int. J. Multiphys., vol. 11, no. 4, pp. 1–20, 2017.

[28] N. Mehreganian and A. Soleiman Fallah, "Blast loading effects on aircraft fuselage," in Multiphysics Simulations in Automotive and Aerospace Applications, 1st ed., M. Moatamedi, T. Rahulan, and H. Khawaja, Eds. London: Elsevier, 2021, p. 301.

[29] N. Jacob, G. N. Nurick, and G. S. Langdon, "The effect of stand-off distance on the failure of fully clamped circular mild steel plates subjected to blast loads," Eng. Struct., vol. 29, no. 10, pp. 2723–2736, 2007.

[30] S. C. K. Yuen and G. N. Nurick, "Deformation and Tearing of Uniformly Blast-Loaded Quadrangular Stiffened Plates," in Structural Engineering, Mechanics and Computation, A. Zingoni, Ed. Oxford: Elsevier Science, 2001, pp. 1029–1036.

[31] G. N. Nurick, S. Mahoi, and G. S. Langdon, "The response of plates subjected to loading arising from the detonation of different shapes of plastic explosive," Int. J. Impact Eng., vol. 89, no. November, pp. 102–113, 2016.

[32] G. N. Nurick and J. B. Martin, "Deformation of thin plates subjected to impulsive loading—A review," Int. J. Impact Eng., vol. 8, no. 2, pp. 159–170, Jan. 1989.

[33] B. Zakrisson, "Numerical Simulations of Blast Loaded Steel Plates for Improved Vehicle Protection," 2013.

[34] W. Zhang, T. Liu, A. Xi, and Y. N. Wang, "Resonant responses and chaotic dynamics of composite laminated circular cylindrical shell with membranes," J. Sound Vib., vol. 423, no. March, pp. 65–99, 2018.

[35] T. Liu, W. Zhang, J. J. Mao, and Y. Zheng, "Nonlinear breathing vibrations of eccentric rotating composite laminated circular cylindrical shell subjected to temperature, rotating speed and external excitations," Mech. Syst. Signal Process., vol. 127, no. July, pp. 463–498, 2019.

[36] T. Liu, W. Zhang, and J. . Wang, "Nonlinear dynamics of composite laminated circular cylindrical shell clamped along a generatrix and with membranes at both ends," Nonlinear Dyn., vol. 90, no. 2, pp. 1393–1417, 2017.

[37] A. S. Fallah, M. Ghajari, and Y. Safa, "Computational modelling of dynamic delamination in morphing composite blades and wings," Int. J. Multiphys., vol. 13, no. 4, pp. 393–429, 2019.

[38] P. Liu, G. Yu, X. Zhu, and Z. Du, "Unsteady aerodynamic prediction for dynamic stall of wind turbine airfoils with the reduced order modeling," Renew. Energy, vol. 69, no. April, pp. 402–409, 2014.

[39] A. Bela, L. Buldgen, P. Rigo, and H. Le Sourne, "Numerical crashworthiness analysis of an offshore wind turbine monopile impacted by a ship," in Analysis and Design of Marine Structures - Proceedings of the 5th International Conference on Marine Structures, MARSTRUCT 2015, 2015, no. 2013, pp. 661–669.

[40] K. Micallef, A. S. Fallah, D. J. Pope, and L. A. Louca, "The dynamic performance of simply-supported rigid-plastic circular steel plates subjected to localised blast loading," Int. J. Mech. Sci., vol. 65, no. 1, pp. 177–191, 2012.

[41] A. S. Fallah, K. Micallef, G. S. Langdon, W. C. Lee, P. T. Curtis, and L. A. Louca, "Dynamic response of Dyneema® HB26 plates to localised blast loading," Int. J. Impact Eng., vol. 73, no. October 2016, pp. 91–100, 2014.

[42] R. Rajendran and J. M. Lee, "Blast loaded plates," Mar. Struct., vol. 22, no. 2, pp. 99–127, 2009.

[43] N. Mehreganian, L. A. Louca, and A. S. Fallah, "DYNAMIC PERFORMANCE OF SIMPLY-SUPPORTED RIGID-PLASTIC SQUARE PLATES SUBJECT TO LOCALISED BLAST LOADING (In press)," J. Eng. Mech., 2018.

[44] C. K. Youngdahl, "Influence of pulse shape on the final plastic deformation of a circular plate," Int. J. Solids Struct., vol. 7, no. 9, pp. 1127–1142, 1971.

[45] K. Micallef et al., "On dimensionless loading parameters for close-in blasts," Int. J. Multiphys., vol. 9, no. 2, p. 193, 2015, [Online]. Available: http://scholar.google.com/scholar?hl=en&btnG=Search&q=intitle:On+dimensionless+loading+parameters+for+close-in+blasts#0.

[46] D. Bonorchis and G. N. Nurick, "The influence of boundary conditions on the loading of rectangular plates subjected to localised blast loading - Importance in numerical simulations," Int. J. Impact Eng., vol. 36, no. 1, pp. 40–52, 2009.

[47] B. M. Dobratz, "Properties of Chemical Explosives and Explosive Simulants," Livermore, 1972.

[48] N. Mehreganian, L. A. Louca, G. S. Langdon, R. J. Curry, and N. Abdul-Karim, "The response of mild steel and armour steel plates to localised air-blast loading-comparison of numerical modelling techniques (Submitted for Publication)," Int. J. Impact Eng., 2017.

[49] G. S. Langdon, W. C. Lee, and L. A. Louca, "The influence of material type on the response of plates to air-blast loading," Int. J. Impact Eng., vol. 78, pp. 150–160, 2015.